

Understanding Phonon Properties in Isoreticular Metal-Organic Frameworks from First Principles

Tomas Kamencek^{1,2}, Natalia Bedoya-Martínez³, and Egbert Zojer¹

¹Institute of Solid State Physics, Graz University of Technology, NAWI Graz, Petersgasse 16, 8010 Graz, Austria

²Institute of Physical and Theoretical Chemistry, Graz University of Technology, NAWI Graz, Stremayrgasse 9, 8010 Graz, Austria

³Materials Center Leoben, Roseggerstraße 12, 8700 Leoben, Austria

ABSTRACT: Metal-organic frameworks (MOFs) are crystalline materials consisting of metal centers and organic linkers forming open and porous structures. They have been extensively studied due to various possible applications exploiting their large amount of internal surface area. Phonon properties of MOFs are, however, still largely unexplored, despite their relevance for thermal and electrical conductivities, thermal expansion, and mechanical properties. Here, we use quantum-mechanical simulations to provide an in-depth analysis of the phonon properties of isostructural MOFs. We consider phonon band structures, spatial confinements of modes, projected densities of states, and group velocity distributions. Additionally, the character of selected modes is discussed based on real-space displacements and we address, how phonon properties of MOFs change, when their constituents are altered, e.g., in terms of mass and spatial extent, bonding structure etc. We find that more complex linkers shift the spectral weight of the phonon density of states towards higher frequencies, while increasing the mass of the metal atoms in the nodes has the opposite effect. As a consequence of the high porosity of MOFs, we observe a particularly pronounced polarization dependence of the dispersion of acoustic phonons with rather high group velocities for longitudinal acoustic modes (around 6000 ms^{-1} in the long wavelength limit). Interestingly, also for several optical phonon modes group velocities amounting to several thousand ms^{-1} are obtained. For heterogeneous systems like MOFs correlating group velocities and the displacement of modes is particularly relevant. Here we find that high group velocities are generally associated with delocalized vibrations, while the inverse correlation does not necessarily hold. These results provide the foundations for an in-depth understanding of the vibrational properties of MOF, and, therefore, pave the way for a future rational design of systems with well-defined phonon properties.

I. INTRODUCTION

Metal-organic frameworks (MOFs) are highly porous structures consisting of metal(-oxide) clusters (the nodes), which are connected by organic molecules (the linkers). The huge variety of organic chemistry renders this material class highly interesting for a number of applications exploiting the high porosity of these structures (e.g. catalysis [1], [2], storage and separation of gases [3]–[6]).

In view of the wide structural and compositional variety of MOFs, vibrational spectroscopy is often used to determine their composition, and to highlight differences in their structural properties [7]–[11]. From a conceptual point of view, infrared or Raman

spectra only relate to phonons at the center of the first Brillouin zone (1BZ), Γ . Conversely, to determine the crystals' (thermodynamic) properties, one needs to include phonons from the entire first Brillouin zone. From those, one can then obtain various practically important quantities, like the heat capacity, elastic constants, thermal expansion coefficients, or the thermal conductivity (where especially the latter two strongly depend on anharmonic effects). Also for charge transport electron-phonon interactions play a decisive role.

All these aspects call for a detailed understanding of phonon properties of MOFs, which is, however, still in its infancy [12], [13]. The situation is further complicated by the enormous number of possible MOF structures,

with the potential that some of them have outstanding properties.

In this work we, therefore, employ state of the art quantum-mechanical simulations to develop first relationships between the phonon properties of MOFs and the nature of their building blocks. As we are at a very early stage of this quest, we focus on the harmonic vibrations of cubic isorecticular MOFs (IRMOFs), i.e. structures with identical linkers along the edges of the cubic repeat units, see Fig. 1(a). In particular, we analyze the relation between the MOF structure (varying linkers and nodes) and quantities like the (projected) densities of states, phonon bands, the degree of localization of specific vibrations, and group velocities. In this way we develop an in-depth understanding of MOF phonon properties.

The paper is organized as follows: We start with an introduction of the studied systems, followed by a detailed description and benchmarking of the applied methodology. In the subsequent section, a general discussion of the phonon density of states will be presented, followed by a detailed analysis of the phonon bands, mode participation ratios, and group-velocity distributions. We mostly focus on the low-frequency regime [below 3 THz (100 cm^{-1})], which is particularly relevant for the materials' thermal properties.

II. STUDIED SYSTEMS

The structure of the considered IRMOFs consists of (comparably heavy) nodes formed by four XO_4 tetrahedra (with X representing a metal), which share one oxygen atom as a common corner. Neighboring nodes are connected by organic molecules via bonds to two oxygen atoms on each side, which results in a cubic pore [see Fig. 1(a)]. Counterintuitively, the primitive unit cells of IRMOFs are not simple cubic (sc), since two neighboring nodes are the mirror images of each other. Thus, two nodes and their respective linkers form the crystallographic basis, which is replicated on a face-centered cubic lattice (fcc).

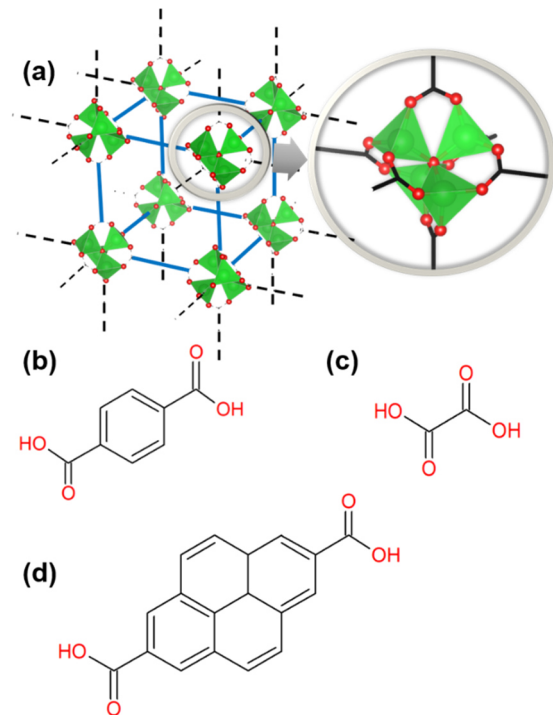


FIG. 1. (a) Exemplary IRMOF geometry in which the linkers have been replaced by blue lines. The nodes, which are shown in the circular insert, consist of four XO_4 ($\text{X} = \text{Mg}, \text{Ca}, \dots$) tetrahedra, which share one oxygen atom. Coloring scheme: X green, O red. (b)-(d): Chemical structures of the studied linker molecules (before deprotonation), which are located between the nodes of the IRMOFs.

The connections in Fig. 1(a) indicated by blue lines represent one of the several possible linker molecules. The chemical structures of the three linkers considered in this study are shown in Fig. 1(b-d): IRMOF-1 [with the linker being shown in Fig. 1(b)] is the most studied IRMOF and, thus, can be viewed as the prototypical IRMOF system. For the Zn-based variant even its phonon band structure has been studied in the context of (negative) thermal expansion [12]. The linker shown in Fig. 1(c) is the shortest possible dicarboxylic acid linker. This renders the system fundamentally relevant. As the resulting MOF lacks a common name, will in the following it will be referred to as IRMOF-130. The small number of atoms in the linker significantly reduces the number of optical phonon modes, which will simplify the following discussion. IRMOF-130 has not been experimentally realized yet, but its Zn-analogue has already been the subject of theoretical studies [14]. As

a third system, we will study IRMOF-14, which is formed by the rather heavy and more extended aromatic dicarboxylic acid linker shown in Fig. 1(d). Being the largest system studied here, it contains 190 atoms in the primitive unit cell, which results in a particularly rich phonon spectrum comprising in total 570 different phonon bands. Notably, IRMOF-14 is characterized by a rather large moment of inertia for rotation around the linker, which ought to profoundly reduce the frequencies associated with torsional vibrations.

Concerning the metal atoms in the node, the Zn-based analogues of IRMOF-1, and -14 are the most commonly investigated structures [12], [15]–[17]. Here, we focus on the less common Mg- (as reference system) and Ca-based systems, which have also been considered in several studies [17]–[20]. The reason for choosing Mg rather than Zn is mostly technical and related to a minor, but still relevant reduction in symmetry, as detailed in the Supplemental Material [21]. For the sake of gaining fundamental insights, the choice of metal atom is, however, rather inconsequential, as the bonding chemistry between metal nodes and linkers has been found to be similar for metal atoms with the same formal charge (oxidation number) [18], [19]. Thus, varying the metal (here, exchanging Mg by Ca) is expected to primarily impact the phonons in a MOF through the different masses of the nodes.

III. METHODOLOGY

A. Density functional theory (DFT) and density functional tight binding (DFTB) calculations

DFT [22], [23] calculations were carried out with the *VASP* code [24]–[27] (version 5.4.1), using the PBE functional [28] and employing the projector-augmented wave method [29] together with the recommended standard potentials [30] (see Supplemental Material [21]). The occupation of electronic states was described with a Gaussian smearing of $\sigma =$

0.05 eV. Projection operators occurring in the non-local parts of the pseudopotentials were evaluated in reciprocal space (`LREAL` tag). The Γ -centered k-mesh and the plane wave energy cutoff were chosen such that the total energy of each system was converged to below 1 meV (a list of parameters for all systems can be found in the Supplemental Material [21]). An energy change of 10^{-8} eV was employed as SCF convergence criterion. The geometries and unit cell parameters of all MOFs were optimized until the maximum force component was below 0.5 meV/Å (see Supplemental Material [21]). In these optimizations, the space group was fixed as $Fm\bar{3}m$.

The above-described DFT calculations were performed for the primitive unit cells of all studied systems. For the extended supercells necessary for studying phonon dispersion relations (see below), such calculations, however, turned out to be prohibitively expensive. Therefore, when calculating off- Γ phonons, the computationally more affordable density functional tight binding (DFTB) approach was used [31]–[34]. This method, despite its approximate character, provides a good compromise between accuracy and efficiency. It has been shown that it yields structural [35] and thermal transport properties [13] of MOFs comparable to the DFT level of theory. The computations based on the self-consistent charge (SCC-)DFTB approach were performed using the *DFTB+* [36] package (version 18.1), and the *3ob-3-1* Slater-Koster files including the *3ob:freq-1-2* extension for obtaining more accurate vibrational properties [37]–[39].

All available angular momentum atomic orbitals were included for each species. When performing calculations on the conventional fcc unit cells, the k-meshes for each system were chosen according to the same convergence criteria as for the DFT calculations (Γ -point or $2\times 2\times 2$, see Supplemental Material [21]). In the case of extended super cell

calculations, only the Γ point was considered for all systems. An SCC convergence criterion of 10^{-10} times the elementary charge was employed. To ensure high-quality geometries, the maximum residual forces in the geometry optimizations were set to 10^{-5} meV/Å.

The third order corrections of the DFTB3 [40] functional were not included, as - compared to the DFT results - they yielded more serious overestimations of the lattice constants than ordinary DFTB. Moreover, the RMS deviations between DFT and DFTB frequencies were found to be slightly larger when including the third order expansion terms in the Hamiltonian (see Supplemental Material [21])

All results reported here were obtained without *a-posteriori* van der Waals (vdW) corrections. This is justified, as the systems of interest consist of covalently and coordinatively bonded constituents. Indeed, tests on IRMOF-130(Mg) show that including van der Waals interactions hardly changes the phonon frequencies (see Supplemental Material [21]); the observed RMS deviation between calculations with and without van der Waals corrections was below 0.05 THz, i.e., below 1.5 cm^{-1} .

B. Phonon properties

Phonons were calculated in reciprocal space by means of lattice dynamics (LD) within the harmonic approximation to the potential energy surface and employing the finite displacement method as implemented in the phonopy [41] code. A displacement amplitude of 0.01 \AA was used, which is also the default value of the code. This choice is motivated by tests on IRMOF-130(Mg), for which changing the displacement to 0.02 \AA or 0.005 \AA yielded RMS deviations below 0.01 THz (0.3 cm^{-1}) for all Γ frequencies. Force constants were symmetrized in the post-treatment with phonopy's internal subroutines, in order to correct for possibly lost symmetries caused by numerical errors. The Γ -phonons for the

comparison between DFT and DFTB were obtained employing primitive unit cells.

Phonon band structure calculations were performed using supercells. For designing these supercells, it is not advisable to start from the primitive unit cell of the fcc lattice, as it is non-orthogonal. This would result in supercells with very different extents in different spatial directions, as discussed in detail in the Supplemental Material [21]. Therefore, we rather used the conventional fcc cells as fundamental building block. Convergence was reached for a $2 \times 2 \times 2$ supercell (see Supplemental Material [21]) for all considered materials. This supercell contains 32 primitive cells. The corresponding supercell for IRMOF-130 is shown in the Supplemental Material [21].

C. Analyzed quantities

Phonon densities of states, band structures, group velocities, and mode participation ratios were used to analyze the relationship between the structural and vibrational properties of MOFs.

Vibrational modes were characterized and compared among systems on the basis of the associated displacement patterns. Technically, this was mostly done by a visual inspection of the corresponding animations considering the symmetries of the vibrations. Additionally, plots of the displacement patterns were created with VESTA 3[42].

The reported densities of states (DOS) were normalized such that integrating over them yields $3N$, where N is the number of atoms in the primitive unit cell.

Less common quantities used in the later discussion are briefly described in the following.

1. Mode participation ratios

A quantitative assessment of the degree of localization of a phonon can be achieved via

the so-called participation ratio (PR) [43]–[45]. It is defined as

$$PR_{\mathbf{q},n} = \frac{\left(\sum_{\alpha=1}^N \frac{|\mathbf{e}_{\mathbf{q},n}^{\alpha}|^2}{m_{\alpha}} \right)^2}{N \cdot \left(\sum_{\alpha=1}^N \frac{|\mathbf{e}_{\mathbf{q},n}^{\alpha}|^4}{m_{\alpha}^2} \right)} \quad (1).$$

Here, \mathbf{q} and n denote the wavevector and band index, N is the number of atoms in the unit cell, $\mathbf{e}_{\mathbf{q},n}^{\alpha}$ are the three components of the vibrational eigenvectors of atom α , and m_{α} is its mass. It is easy to show from Eq. (1) that when the PR is on the order of $1/N$, the mode is considered to be highly localized (only few atoms move), whereas participation ratios on the order of 1 mean that the mode is highly delocalized (essentially all atoms in the unit cell move with the same amplitude). Since the eigenvectors depend on \mathbf{q} , the participation ratio can vary significantly within a band.

2. Frequency and group velocity resolved density of states

For phonon transport, the group velocities of the phonons are amongst the most relevant parameters, as they determine the time scales on which phonons propagate and exchange energy. Unfortunately, the sheer number of bands in MOFs makes an in-depth discussion of each of them together with the associated group velocities virtually impossible. A strategy for still being able to discuss trends in band dispersions and group velocities relies on calculating the density of states resolved not only with respect to ω , but also with respect to the norm of the group velocity vector, $\|\mathbf{v}_{\mathbf{g}}\|$. We define this 2D density function in analogy to the common definition of the DOS as

$$p(\omega, \|\mathbf{v}_{\mathbf{g}}\|) = \frac{1}{3N N_{\mathbf{q}}} \sum_{\mathbf{q},n}^{N_{\mathbf{q}},3N} \delta(\omega - \omega_{\mathbf{q},n}) \delta(\|\mathbf{v}_{\mathbf{g}}\| - \|\mathbf{v}_{\mathbf{g}}\|_{\mathbf{q},n}) \quad (2)$$

The prefactor in Eq. (2) contains the number of bands ($3N$) and the number of wavevectors $N_{\mathbf{q}}$ used in the discrete sampling of the phonon bands in the 1BZ. In this way, the density function p is normalized to 1. The 2D density function shows, how frequently certain values of the group velocities occur at a given

frequency. In practice, the δ distributions are replaced by Gaussian or Lorentzian functions with a finite width. Here, widths of 0.2 THz and 0.2 THzÅ were used for the (P)DOS and for the group velocity resolved DOS. In both cases, for sampling the 1BZ a uniform \mathbf{q} -mesh containing 20x20x20 points was applied.

IV. RESULTS AND DISCUSSION

A. Validation of the DFTB approach

As a first step, it is important to benchmark the accuracy of the DFTB calculations against the more reliable DFT results. This is done for the unit-cell parameters and for the vibrations at the Γ -point.

TABLE I: Comparison of the optimized lattice constants, a , obtained within DFT (VASP) and DFTB (DFTB+). Additionally, the root-mean-square deviations between the frequencies for modes up to 5 THz ($RMS_{\leq 5 \text{ THz}}$) and for all modes (RMS_{full}) are shown.

IRMOF	1(Mg)	130(Mg)	130(Ca)	14(Mg)
$a_{DFT} / \text{Å}$	13.10	8.82	9.62	17.35
$a_{DFTB} / \text{Å}$	13.16	8.84	9.46	17.45
$\Delta a / a_{DFT} / \%$	0.46	0.23	-1.66	0.59
$RMS_{\leq 5 \text{ THz}} / \text{THz (cm}^{-1}\text{)}$	0.10 (3)	0.15 (5)	0.38 (12)	0.08 (3)
$RMS_{full} / \text{THz (cm}^{-1}\text{)}$	1.25 (42)	1.19 (40)	1.29 (43)	1.08 (40)

Table I shows that for the Mg-based MOFs the equilibrium lattice constants obtained with the two approaches deviate by less than 0.6 %. Also for the Ca-based MOF, the observed deviations ($< 2\%$) are at an acceptable level. Moreover, the agreement between the frequencies at the Γ -point calculated with DFT and DFTB is satisfactory, as can be seen in Fig. 2(a) and (b) for IRMOF-1(Mg). Equivalent plots for IRMOF-130(Mg/Ca) and IRMOF-14(Mg) can be found in the Supplemental Material [21].

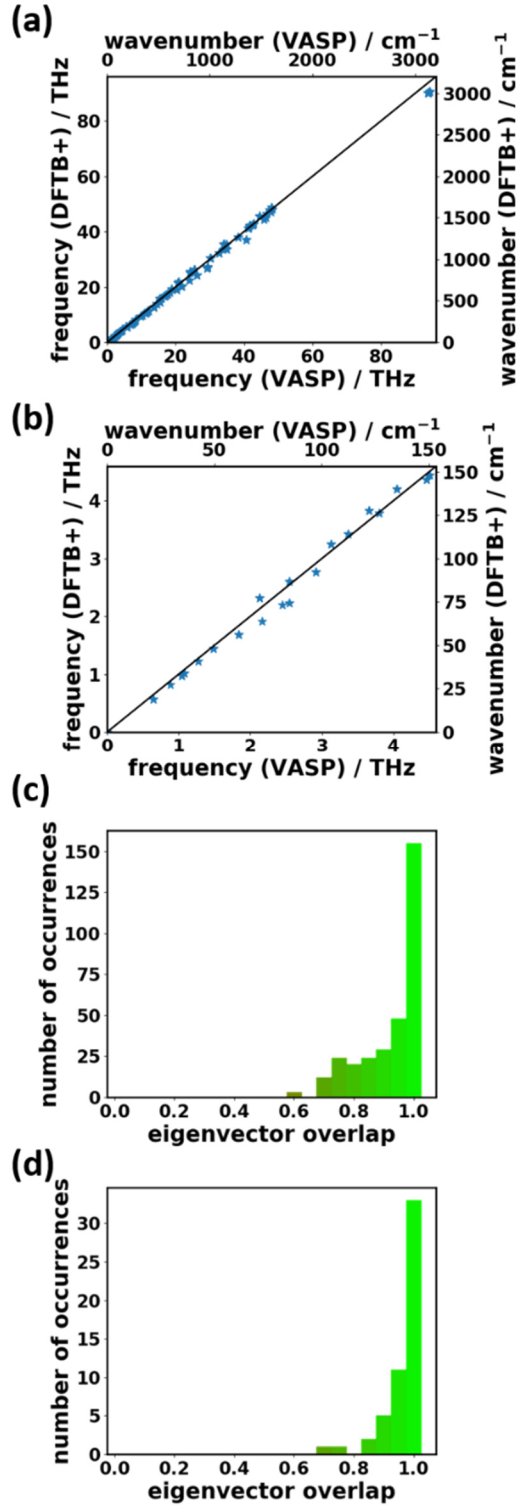


FIG. 2. Scatter plots of the Γ frequencies obtained with VASP and DFTB+ for IRMOF-1(Mg) in (a) the full frequency range and (b) for a reduced range comprising modes up to 5 THz. (c) and (d) show histograms of the scalar products between eigenvectors obtained with VASP and DFTB+ for (c) all modes and (d) modes with frequencies ≤ 5 THz.

The deviations are clearly larger in the high-frequency than in the low-frequency region,

which is confirmed by the corresponding RMS values in Table I. The distinction between the two spectral ranges is insofar relevant, as for physical properties derived from the phonons usually the lower lying modes are more important, as they are the ones that are thermally occupied.

As a final benchmark, the eigenvectors of the dynamical matrix are compared between DFT and DFTB. As the dynamical matrix is Hermitian, its eigenvectors form an orthonormal basis, which allows an analysis of pairwise scalar products between them. The majority of the scalar products amounts to ~ 1 (perfect agreement) or to slightly smaller values [see Fig. 2(c) and (d)]. Again, a better overall agreement is obtained at smaller frequencies.

These data suggest that, especially in the low-frequency region, deviations between DFT and DFTB are so small that we can confidently base the following discussion on the DFTB results.

B. Impact of structural variations on the phonon density of states

The densities of states projected onto the various atomic species are the ideal starting point for the discussion of the phonon properties of the MOFs introduced in Sec. II. They allow a first assessment of the frequency ranges in which phonon modes exist in each of the materials. Moreover, they show, at which frequencies certain types of atoms primarily contribute to the oscillations. The PDOSs of IRMOF-130(Mg/Ca), IRMOF-1(Mg), and IRMOF-14(Mg) are shown in Fig. 3(a) for the entire frequency range. A zoom into the frequency region up to 20 THz is shown in Fig. 3(b). The contributions from different atom types are plotted in a stacked manner, such that the outermost contour corresponds to the total DOS.

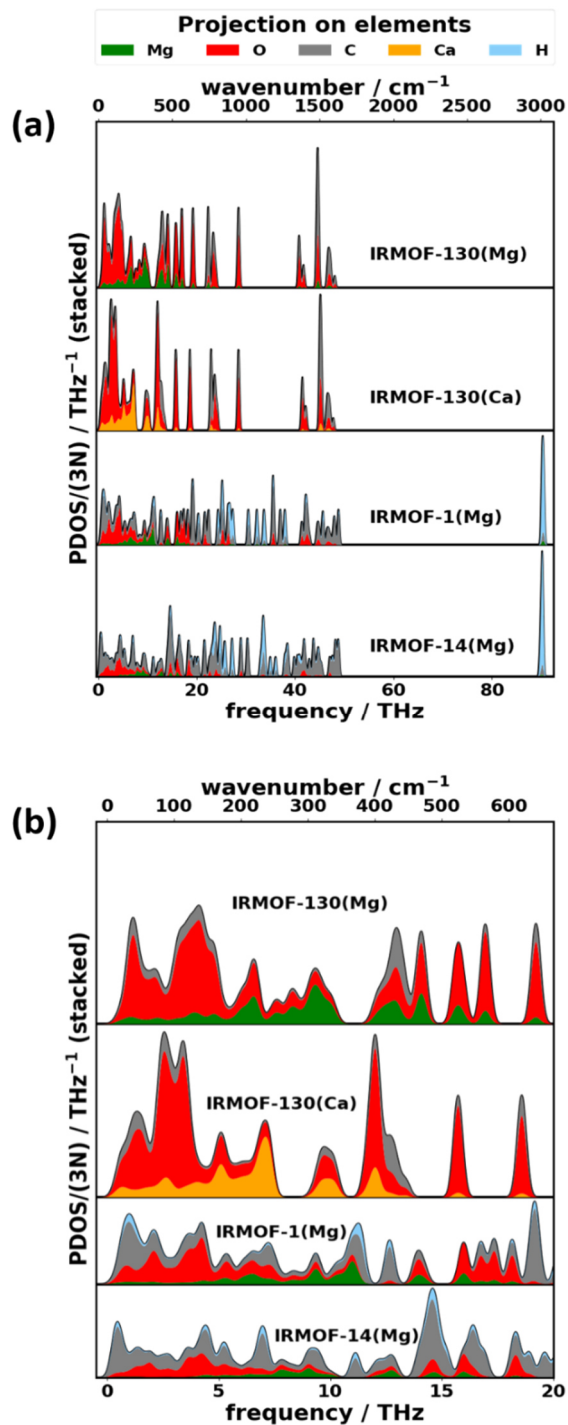


FIG. 3. Projected density of states (PDOS) normalized to the number of bands as a function of frequency for IRMOF-130(Mg), IRMOF-130(Ca), IRMOF-1(Mg), and IRMOF-14(Mg). The PDOS contributions per species are plotted in a stacked way so that the outermost line represents the total DOS. Panel (a) shows the entire spectral range, while panel (b) displays a zoom into the low-frequency region up to 20 THz.

Especially at higher frequencies, the phonon DOSs of all systems are dominated by rather sharp peaks. This suggests mostly weakly

dispersing bands. For IRMOF-1(Mg) and IRMOF-14(Mg), the highest-frequency modes occur around 90 THz. These vibrations correspond to C-H stretching motions, as can be concluded from analyzing their eigenvectors. Thus, they do not have equivalents in IRMOF-130, where the linkers do not contain any H atoms. In all systems, the region between 40 and 50 THz is dominated mostly by stretching vibrations of the carbon and oxygen atoms in the linkers with contributions from hydrogen bending vibrations in IRMOF-1(Mg) and IRMOF-14(Mg). The non-vanishing participation of metal atoms in the higher frequency vibrations in IRMOF-130(Mg/Ca) is attributed to the very short lateral extent of the linkers in those systems.

In the region between 29 and 40 THz a wide phonon band gap opens in IRMOF-130(Mg) and IRMOF-130(Ca). Conversely, for IRMOF-1(Mg) and IRMOF-14(Mg) this spectral region is dominated by in-plane bending vibrations of the aromatic linker moieties. Especially in IRMOF-14, the high number of atoms in the linker results in many optical phonon branches almost closing the entire band gap observed in IRMOF-130.

C-H out-of-plane bending modes dominate the next series of bands between 23 and 27 THz in IRMOF-1(Mg) and IRMOF-14(Mg). Some modes in that spectral range also correspond to in-plane deformations of the entire linkers. These are the only modes showing up in that frequency range in IRMOF-130(Mg/Ca).

These considerations show that the spectral region above ~ 20 THz essentially represents vibrations localized in the linkers with only small contributions from the metal atoms.

Below 20 THz, oscillations of the metal atoms increasingly contribute to the phonon density of states. In that spectral range, coupled oscillations of linkers and nodes dominate. At very low frequencies (below ~ 3 THz) the contributions of the metal atoms in IRMOF-1 and IRMOF-14 decrease. This indicates that

vibrations in that region are again largely localized in the linkers. They, for example, comprise torsional motions of the aromatic systems, as will be discussed in more detail below, when analyzing selected optical phonon bands. The low-frequency modes are particularly relevant, as they are occupied already at low temperatures ($k_B T$ corresponds to ~ 6 THz).

Interestingly, below a certain frequency [~ 10.5 THz for IRMOF-130(Mg) and IRMOF-14(Mg); ~ 7.8 THz for IRMOF-130(Ca); ~ 12.0 For IRMOF-1(Mg)], there are enough, sufficiently dispersing phonon modes to form a *continuous* DOS without band gaps. This has, for instance, practical implications for phonon transport: a continuous DOS with a multitude of weakly dispersing bands in the same spectral region makes inter-phonon scattering processes more likely, as it eases the simultaneous conservation of energy and momentum in scattering events.

The choice of the metal atom contained in the nodes has a particularly large effect in the spectral region up to 20 THz [i.e., the region shown in Fig. 3(b)], as can be inferred from comparing IRMOF-130(Mg) and IRMOF-130(Ca). For the nearly twice as heavy Ca atom in the linkers, the various PDOS features (including the phonon band gaps) shift to distinctly lower frequencies. Such shifts are expected considering the dependence of resonance frequencies on the mass of the oscillating objects. The observation that the shift mostly affects the modes at lower frequencies (up to ~ 20 THz) is consistent with the above-discussed finding that motions of the metal atoms primarily contribute to vibrations in that spectral region.

Further insight regarding the spectral region most strongly affected by changing the metal atom can be obtained by comparing the (normalized) cumulative DOS (i.e., the integrals over the DOS up to a certain frequency). Fig. 4 shows a comparison for IRMOF-130(Mg) and IRMOF-130(Ca). Below

~ 20 THz the cumulative DOS of IRMOF-130(Ca) is larger (or equal) to that of its Mg-based analogue. This difference essentially disappears for higher frequencies.

The normalized cumulative DOS also provides insight into how the complexity of the linker affects the spectral distribution of phonon modes. Comparing the situations for IRMOF-130 and IRMOF-1(Mg) in Fig. 4, one sees that in the latter case the normalized cumulative DOS rises more gradually. This implies that the spectral distribution in IRMOF-1 is shifted to higher frequencies. This observation can be rationalized by the more extended linkers, which give rise to an increasing number of intra-linker modes, which, as discussed above, are typically found at higher frequencies. This trend is further amplified for IRMOF-14.

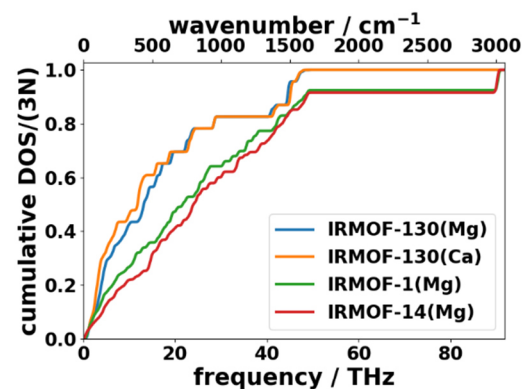


FIG. 4. Normalized cumulative DOS, i.e., DOS integrated up to a given frequency, as a function of that frequency divided by the number of bands.

C. Discussion of the (low frequency) band structures

While the DOSs discussed so far are useful for obtaining a general overview of the spectral regions in which certain vibrations occur, further insight can be gained by analyzing the associated phonon band structures. Owing to the huge number of optical phonon modes in all considered MOFs, we will restrict the following discussion to a frequency range of up to 3 THz (i.e., 100 cm^{-1}). Even in that region the number of phonon bands is huge, as is shown in Fig. 5. This is the consequence of the significant number of atoms in the primitive unit cells (46 for IRMOF-130, 106 for IRMOF-1,

and 190 atoms for IRMOF-14). For IRMOF-1(Mg), we find good qualitative agreement with the band structure of IRMOF-1(Zn) reported in [12].

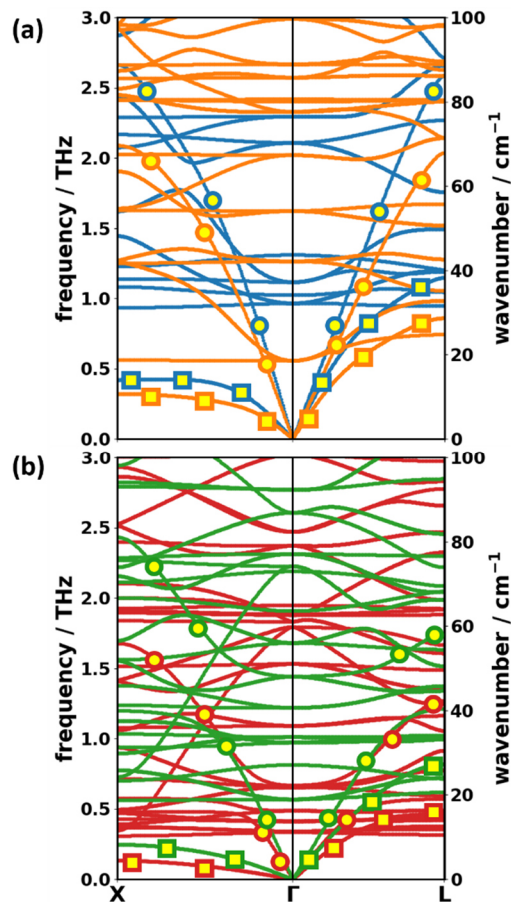


FIG. 5. Phonon band structure of (a) IRMOF-130(Mg) (blue) and IRMOF-130(Ca) (orange) and (b) IRMOF-1(Mg) (green) and IRMOF-14(Mg) (red). Γ -X: direction corresponding to the linker axis in real space, Γ -L: direction corresponding to the space diagonals in real space. The round (square) markers show the longitudinal (transversal) acoustic bands.

In the following discussion, we first focus on the acoustic bands. Along the linker direction (Γ -X), the twofold degenerate transverse acoustic (TA) bands (the bands lowest in energy marked by squares in Fig. 5) displays a significantly smaller dispersion than the longitudinal acoustic (LA) band (marked by circles in Fig. 5). The difference in dispersion can be explained considering the porous structure of the MOFs: For longitudinal acoustic waves all atoms are displaced in a direction of high atomic densities. I.e., LA vibrations in Γ -X direction correspond to

compressions and expansions of the “chain” formed by linkers and nodes. Conversely, TA phonons propagating in Γ -X cause a displacement of the linkers towards the open pores. This is associated with a smaller restoring force and, consequently, with a reduced band dispersion. This reasoning is also consistent with the observation that the difference between longitudinal and transverse modes decreases along the space diagonal of the pore (Γ -L). An interesting implication of this finding is that the frequency of the TA modes along Γ -X should increase upon filling the pores of the MOFs by guest or solvent molecules.

For both IRMOF-130 based systems it is possible to follow the acoustic bands from the Γ point to the boundary of the 1BZ [see Fig. 5(a)], which allows to estimate the corresponding band width. In the Γ -X direction, for the Mg-based system it amounts to approx. 2.66 THz for the LA mode and to 0.42 THz for the TA modes. Consistent with the discussion in the previous section, these band widths decrease when replacing Mg by Ca (to 2.08 THz and 0.32 THz, respectively). Along the Γ -L direction, the band widths decrease slightly for the longitudinal mode (2.58 THz and 2.03 THz for IRMOF-130(Mg) and IRMOF-130(Ca), respectively). Conversely, for the transverse modes the band widths more than double compared to Γ -X (to 1.14 THz and 0.86 THz). This is in line with the above discussion of restoring forces. For IRMOF-1(Mg) and IRMOF-14(Mg) the situation is more involved, as there one encounters avoided band crossings. Analyzing the symmetry of the displacements associated with the phonons at different wavevectors, we are able to identify the parts of the bands with the same character. In Fig. 5(b) the sections corresponding to vibrations with the same character as the longitudinal acoustic bands close to the Γ -point are highlighted by circles.

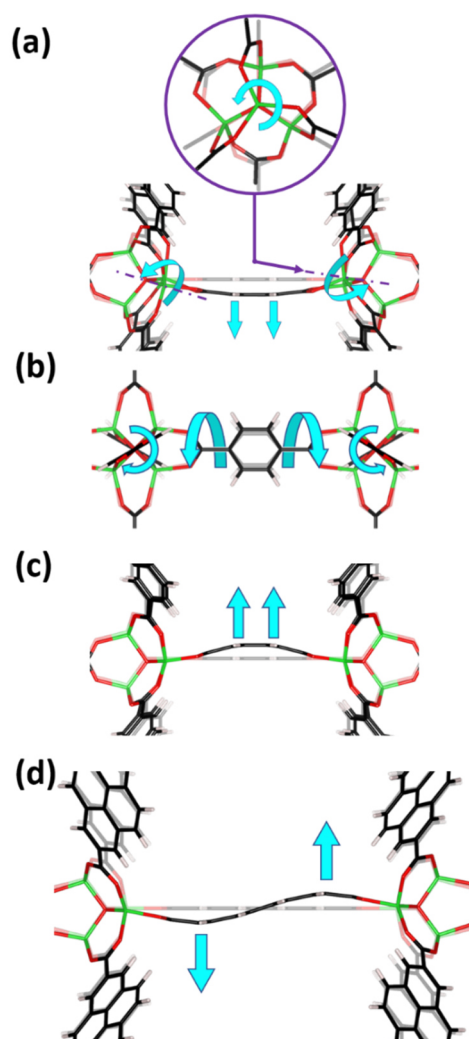


FIG. 6. (a-c) Displacement patterns of low frequency optical modes in IRMOF-1(Mg). (a) Twisting mode of MgO₄ tetrahedra around an axis spanned by the central oxygen atom and the associated magnesium atom at 0.57 THz (19 cm⁻¹) inducing a bending also in the linkers ([110] view; circle: [111] view). (b) Linker torsion around molecular axis at 0.81 THz (27 cm⁻¹) ([100] view), and (c) pure linker bending vibration at 1.44 THz (48 cm⁻¹) ([110] view). (d) Displacement pattern of a second order bending mode in IRMOF-14(Mg) at 1.79 THz (60 cm⁻¹) ([110] view). The undisplaced geometry is drawn with decreased intensity in the back. Coloring scheme: C black, Mg green, O red, H white. The amplitudes were exaggerated for reasons of clarity. Frequencies are given for the Brillouin zone center.

Nevertheless, the avoided crossings render a sensible determination of the widths of the LA band in IRMOF-1(Mg) impossible. For the TA bands in the Γ -X direction avoided crossings cannot occur as this band is the lowest in energy along the entire \mathbf{q} -path. Thus, in this case a band width can be determined (0.25 THz), which is smaller than for both,

IRMOF-130(Mg) and IRMOF-130(Ca). Not unexpectedly, in IRMOF-14(Mg), with a further increased number of optical bands (already below 0.5 THz), the situation becomes even more complex. Nevertheless, also here a band width for the TA bands along Γ -X can be determined. With 0.13 THz it is by far the smallest of all considered systems. We attribute this decrease in band width of the TA modes with linker complexity to a decreased resistance of the longer and more flexible linkers to transverse distortions.

As far as the optical modes are concerned, their sheer number is too large to discuss all of them in full detail. Therefore, in the following we will describe a few representative examples. In all studied systems, the optical phonon mode with the lowest frequency corresponds to a bending motion of the linkers [see Fig. 6(a)]. In that mode, the metal atoms are essentially frozen while the linker molecules together with the oxygens move. The animation of the corresponding vibration reveals that the XO₄ (X = Mg, Ca) tetrahedra twist around an axis through the central O atom of the node and the associated metal atom. The linkers follow the motion of the nodes. The low frequency of the mode implies that the restoring force triggered by the vibration is rather weak.

The next mode in IRMOF-1(Mg) at approximately 0.81 THz (27 cm⁻¹) corresponds to a torsional mode, in which the entire aromatic ring undergoes rigid twisting around the long axis of the linker with only little involvement of the oxygens [see Fig. 6(b)]. The equivalent mode in IRMOF-14(Mg) occurs already at 0.34 THz (11 cm⁻¹). The significant shift of this mode in the latter system can be explained by the much higher torsional moment of inertia of the more extended linker. This rationale works even quantitatively: the torsional moment of inertia of the twisting moiety (C and H atoms of the linkers) in IRMOF-14 amounts to 509 uÅ² (with u being the atomic mass unit), while it is only 89.9 uÅ² for IRMOF-1. As the resonance

frequency of a torsional oscillator scales with one over the square root of the moment of inertia, the frequency of the mode should decrease by a factor of 2.38 for IRMOF-14 compared to IRMOF-1. This is exactly the ratio of the torsional frequencies in the full calculations on the two MOFs.

The next higher modes are related to those shown in Fig. 6(a) and (b), albeit with varying phase shifts between linkers or with displacements affecting only individual linkers. A more detailed discussion of these modes is not instructive, as considering their near degeneracy, it cannot be excluded that different solutions within the resulting “sub-space” of displacements occur upon changing the numerical details of the diagonalization of the dynamical matrix.

The next fundamentally different mode is found at 1.44 THz (48 cm^{-1}) in IRMOF-1, and at 0.67 THz (22 cm^{-1}) in IRMOF-14. It is characterized by a bending vibration of the linker, as shown in Figure 6(c). For the longer linker in IRMOF-14, also a second order bending vibration is present in the low-frequency region at 1.79 THz (60 cm^{-1}). The corresponding displacement pattern is shown in Fig. 6(d). In passing we note that localized vibrations like those discussed so far are often referred to as rigid unit modes (RUMs [46]), in which entire building blocks of a MOF move rigidly. RUMs of that kind have been used to describe the elastic behavior [9] or the negative thermal expansion coefficient in IRMOFs [47]–[51] (in addition to mechanism related to acoustic phonon softening [12]).

Another type of mode that should be mentioned here (as it will become relevant for the discussion in the next section) is characterized by a torsional motion of the carboxylic oxygens around the linker axis (see Fig. 7). In IRMOF-1 and IRMOF-14 such modes occur at essentially the same frequency at Γ ($1.91\text{ THz} = 64\text{ cm}^{-1}$ in IRMOF-1, $1.95\text{ THz} = 65\text{ cm}^{-1}$ in IRMOF-14). In IRMOF-130(Mg) and IRMOF-130(Ca) the corresponding modes are

found at 1.31 THz and 2.41 THz, respectively. A variant of these modes in which also the metal atoms bonded to the carboxylic oxygens participate in the torsional motion are found at 2.30 THz in IRMOF-130(Mg) and at 2.02 THz in IRMOF-130(Ca). Interestingly, the frequencies of the former modes are higher in the Ca- than in the Mg-based MOF, although typically the larger mass of the metal atom results in a shift of the peaks in the opposite direction. We explain this behavior for the torsional motion of the oxygens by the steeper torsional potential we calculate for the Ca-based system (see Supplemental Material [21]); i.e., this effect is not related to the mass of the metal atoms but rather to their bonding properties.



FIG. 7. Displacement pattern of a typical optical mode in which the carboxylic oxygens oscillate around the linker axis, while the rest of the systems does not move. Such modes occur in all systems (e.g. at 1.91 THz (64 cm^{-1}) in IRMOF-1(Mg)) at Γ ([100] view). The undisplaced geometry is drawn with decreased intensity in the back. Coloring scheme: C black, Mg green, O red, H white. The amplitudes were exaggerated for reasons of clarity.

D. Localization of vibrations

A central question for the phonon properties of MOFs is to what extent certain vibrations are localized on individual components (e.g. linkers or nodes). The degree of localization can be quantified by the mode-participation ratios, PRs, defined in Sec. III, where a participation ratio of 1 denotes a fully delocalized mode, while small participation ratios denote strong localization. Phonon band structures colored according to the mode participation ratios are shown in Fig. 8 for all investigated systems along a closed path of high symmetry directions.

A general observation is that the strongly dispersing bands are characterized by high PRs with essentially all atoms participating in the respective oscillations. This is not surprising, considering that non-zero wavevectors refer to

phase shifts of the displacements between different unit cells. These significantly impact the energy of a phonon only, if the motions in different unit cells couple to each other. This requires a certain degree of delocalization of the mode. The only rather strongly dispersing band with a comparably small participation ratio is the LA band in Γ -K direction in IRMOF-130 (Mg/Ca) in the vicinity of the avoided crossing between 1.0 THz and 1.5 THz.

Notably, the opposite correlation does not hold. I.e., there are multiple bands, which are essentially flat (at least for a certain range of wave vectors), but for which the PRs are large. Close to the Brillouin-zone boundaries, this can be understood from the “standing-wave” nature of the corresponding oscillations, which diminishes the band dispersion even if many atoms in the unit cell oscillate. This explanation, however, does not apply to all weakly dispersing bands with high participation ratio. For instance, the flat band at 2.3 THz (2.0 THz) in IRMOF-130(Mg) [IRMOF-130(Ca)] has a PR of 0.72 (0.86). The reason for that lies in the peculiarities of the atomic displacements associated with these modes. As mentioned in Sec. IV C, the modes in question correspond to torsional vibrations of the carboxylic oxygens together with the atoms in the metal linkers. Due to the short linker, this involves nearly all atoms of the MOF, which explains the high participation ratio. In the absence of hydrogen atoms in the linker, the torque generated by the torsion is, however, not transmitted through the carbon single bond that connects two adjacent nodes. Thus, a phase-shift between torsional motions of carboxylic groups in neighboring nodes hardly affects the phonon energy, which results in flat bands.

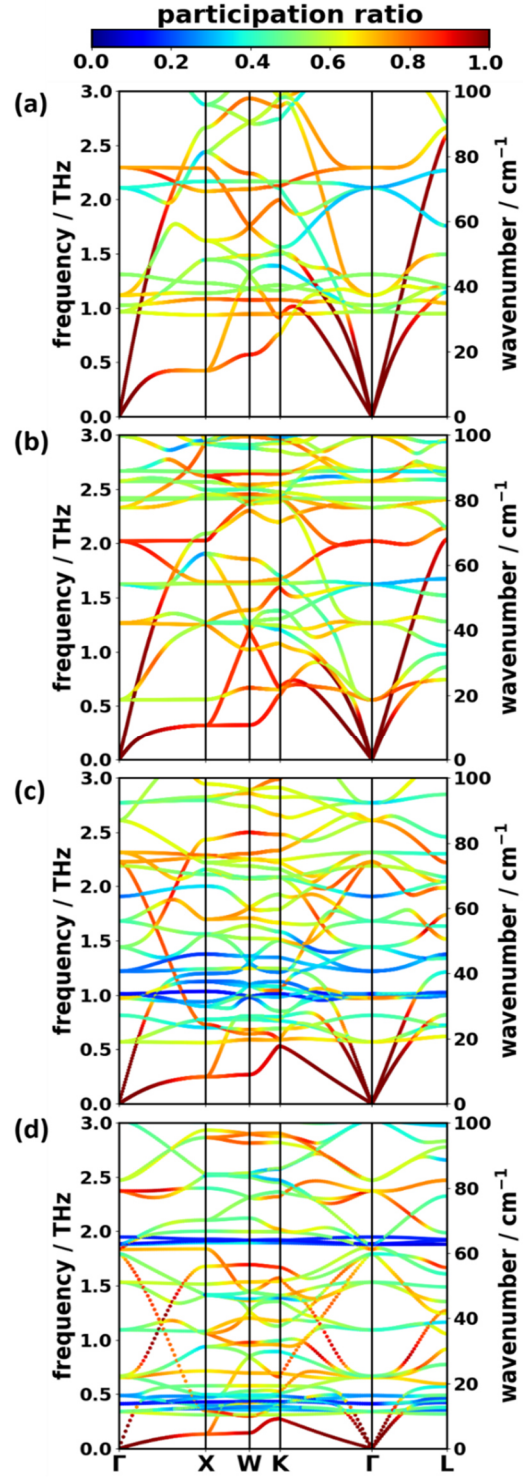


FIG. 8. Phonon band structures of (a) IRMOF-130(Mg) (b) IRMOF-130(Ca), (c) IRMOF-1(Mg), and (d) IRMOF-14(Mg) zoomed in the very low frequency region, colored according to the mode participation ratios. Γ -X: direction corresponding to the linker axis in real space, Γ -K: direction corresponding to the face diagonals in real space; Γ -L: direction corresponding to the space diagonals in real space.

As far as the other phonon modes discussed in Sec. IV C are concerned, we focus on the case

of IRMOF-1 at Γ . The two modes starting at 0.57 THz display a rather large participation ratio (0.64), which can be explained by the fact that for those modes all atoms except the metal atoms and the central oxygens move. Conversely, the nodes do not move significantly in the linker torsion and bending mode at 0.81 THz and 1.44 THz. Therefore, the associated PRs are smaller (0.41 and 0.43 at Γ). The participation ratio of the mode at 1.91 THz is even smaller (0.23) as here only the carboxylic oxygens of the linker move. The pronounced localization of this oscillation and the equal amplitudes of the motions of all carboxylic oxygens results in a participation ratio that equals the ratio between the number of carboxylic oxygens and the total number of atoms in the MOF (which also amounts to 0.23). In IRMOF-14, similar displacement patterns can be held responsible for the bands with particularly low participation ratios between approx. 0.3 THz and 0.6 THz.

E. Phonon group velocities

An important phonon property that can be directly extracted from the gradient of the band structures is the group velocity. It is of distinct relevance for many transport processes, as it quantifies the speed at which thermal energy is transported by a given phonon. Coloring the phonon bands of the investigated systems according to their group velocities (Fig. 9), it becomes apparent that longitudinal acoustic modes have by far the highest group velocities in the low frequency region. This is consistent with the notion that MOFs most strongly resist a longitudinal compression. As indicated already in Sec. IV C, the group velocities of the transverse acoustic phonons are significantly smaller, especially for modes propagating in the Γ -X direction.

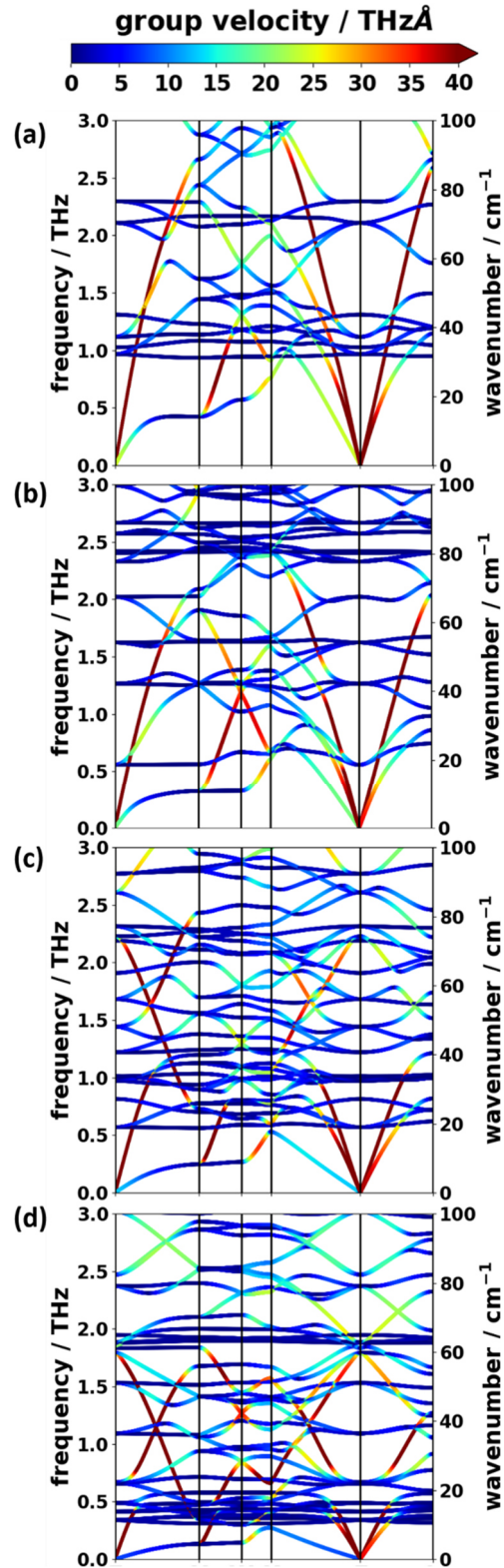


FIG. 9: Phonon band structures of (a) IRMOF-130(Mg), (b) IRMOF-130(Ca), (c) IRMOF-1(Mg), and (d) IRMOF-14(Mg) zoomed in the very low frequency region, colored according to the norm of the group velocities. The group velocity scale was truncated at 40 THzÅ for reasons of visibility. Γ -X: direction corresponding to the linker axis in real space, Γ -K: direction corresponding to the face diagonals in real space; Γ -L: direction corresponding to the space diagonals in real space.

To assess the role played by the structure of the MOFs, as a first step, we analyze the group velocities of the acoustic modes in the long-wavelength limit (i.e., for $\mathbf{q} \rightarrow 0$). They correspond to the respective speeds of sound, c . Interestingly, as shown in Fig. 10(a), we find that for the majority of the propagation and displacement directions the values of c only weakly depend on the linker [see, e.g., slopes of the fitted straight lines listed left of the data points in Fig. 10(a)]. Heavier metals in the node (Ca vs. Mg) somewhat reduce c , but the effect is not particularly strong. The only two types of modes for which c significantly depends on the structure of the MOF are the (degenerate) transverse acoustic modes in the Γ -X directions and one of the transverse acoustic modes in the Γ -K direction (the one characterized by a displacement perpendicular to the face of the cube within which the wave propagates).

To rationalize the only very weak dependence of the speed of sound on the MOF structure, it is useful to consider the example of a 1D chain of masses, m , separated by a distance, a , and elastically coupled by a force constant, γ . In this case, one obtains the following expression for c :

$$c = a \sqrt{\frac{\gamma}{m}} \quad (3)$$

A similar relation holds for cubic crystals along high-symmetry directions [52]. Multiplying Eq. (3) by the mass density, $\rho = m/a^3$, one obtains:

$$c \cdot \rho = \sqrt{\gamma m} \frac{1}{a^2} \quad (4)$$

Interestingly, when plotting $c \cdot \rho$ as a function of a^{-2} , or the respective square roots [see Fig. 10(b)], one obtains an essentially linear relationship. In the spirit of Eq. (4), this suggests that the product of stiffness times inertia, $\sqrt{\gamma m}$, is constant throughout all studied systems. In other words, increasing the size of the linker changes the mass of the unit cell, but simultaneously decreases the effective stiffness of the system. Consequently, in the argument of the square root of Eq. (3), the numerator decreases while

the denominator increases with the size of the linkers. Longer linkers, however, also result in an increase of the unit-cell length, a , which cancels the decrease in $\sqrt{\gamma/m}$. The compensation works best for modes with a speed of sound around 6000 ms^{-1} [as exemplified by the slopes k of the linear fits in Fig. 10(a)]. For modes with a smaller value of c , the speed of sound decreases with linker length, where the magnitude of the effect is amplified for larger deviations from $c \approx 6000 \text{ ms}^{-1}$.

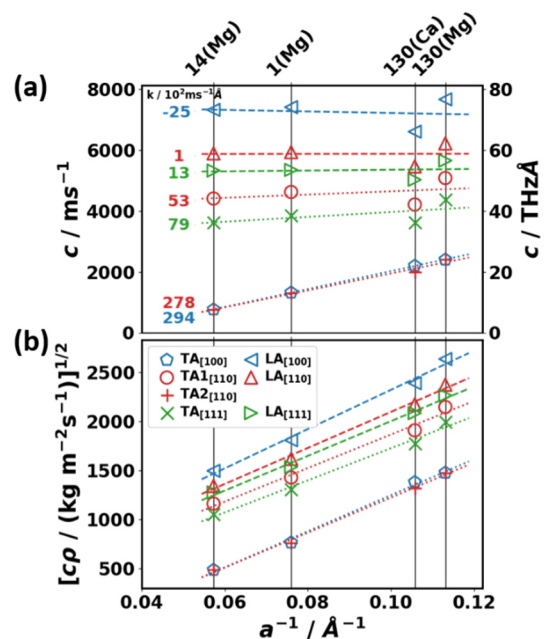


FIG. 10. (a) Dependence of the speed of sound for different directions and polarizations on the MOF structure. For consistency with panel (b) the structure of the MOF is characterized by the inverse unit cell length. The straight lines are linear fits through the respective data points. The slopes, k , of those fits are given left of the lines in units of $10^2 \text{ms}^{-1}\text{\AA}^{-1}$. An equivalent plot (and equivalent fits) for a linear length scale can be found in the Supplemental Material [21]. Notably, whether c is plotted as a function of a or of a^{-1} does not qualitatively change the situation. (b) Square roots of group velocities times mass densities as a function of a^{-1} for the same modes as in panel (a). The dashed and dotted straight lines are again linear fits. The pentagon, circle, and two crosses denote the transversal acoustic modes, where the two modes are degenerate for the Γ -X and Γ -L directions. The different triangles denote longitudinal acoustic modes.

Regarding the group velocities of the optical modes, the situation is again rather complex due to their high number. Thus, to analyze the

overall situation, we resort to densities of states in analogy to Sec. IV B. Correspondingly, Fig. 11 shows such densities of states, which now are resolved not only with respect to ω , but also with respect to the norm of the group velocity vector (see Sec. III). Several conclusions can be drawn from these densities:

(i) The modes with the highest group velocities for all MOFs are found below 3 THz. Fig. 11 shows that they can be associated with the longitudinal acoustic phonon branches. In that region, group velocities beyond 60 THzÅ (i.e. 6000 ms⁻¹) are reached. These values are comparable to those observed in many non-porous materials, which is consistent with the finding that the porosity of the materials primarily impacts the transverse modes.

(ii) Interestingly, in all systems also in the region of the optical phonons, one observes group velocities amounting to several ten THzÅ. In fact, for IRMOF-1 and IRMOF-14 there is a pronounced peak around 10 THz. Such “fast” optical phonons will be thermally occupied at room temperature (there, 10 THz corresponds to $\sim 1.7 k_B T$). This suggests that their contribution to processes like thermal transport can be significant. Notably, in all systems there are also significantly dispersing bands between 40 THz and 50 THz, where we find the backbone stretching vibrations of the linkers.

(iii) In spite of the very high group velocities observed in Fig. 11, the densities of the associated phonons are several orders of magnitude smaller than those of phonons with group velocities of only a few THzÅ. This is not well resolved for the logarithmic density scales chosen for all panels in Fig. 11. Therefore, in Fig. 12, we show the normalized density of group velocities in a linear plot. That quantity is obtained by integrating the data from Fig. 11 over all frequencies (see Supplemental Material [21]).

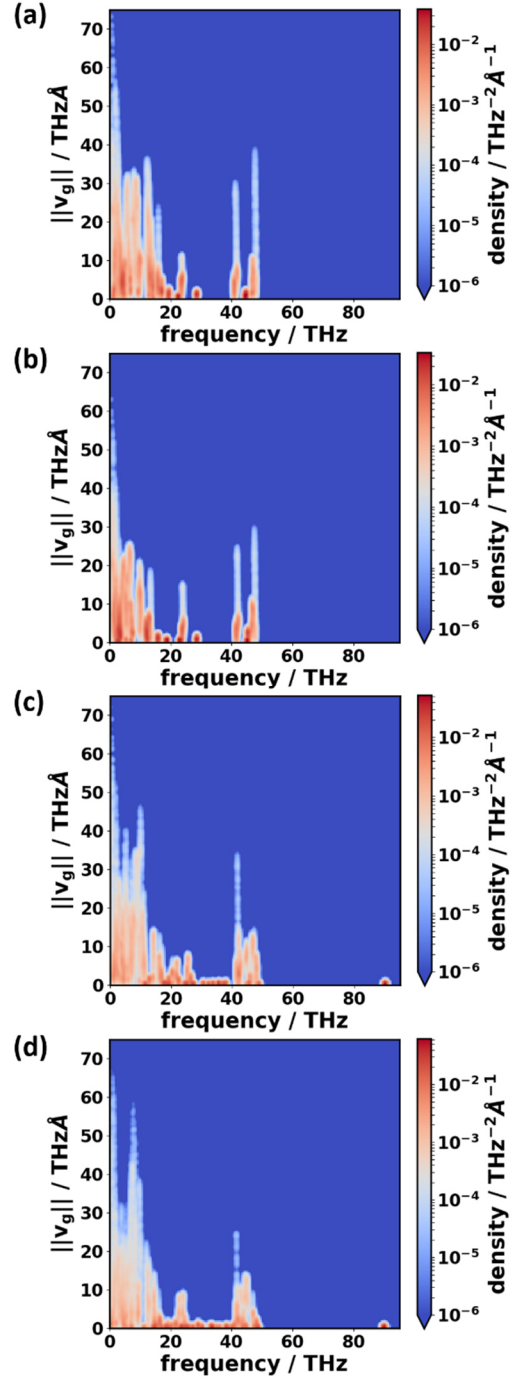


FIG. 11. Normalized frequency and group velocity resolved DOS of (a) IRMOF-130(Mg), (b) IRMOF-130(Ca), (c) IRMOF-1(Mg), and (d) IRMOF-14(Mg). A high density indicates that many modes with that frequency and group velocity can be found in the evenly sampled 1BZ.

(iv) The data in Fig. 12 support the qualitative statements from (i)-(iii). They, however, show that upon increasing the length of the linkers, modes with particularly small group velocities increasingly dominate. Moreover, a comparison between IRMOF-130 (Mg) and IRMOF-130(Ca) shows that increasing the mass

of the metal atoms also reduces the most frequent group velocities.

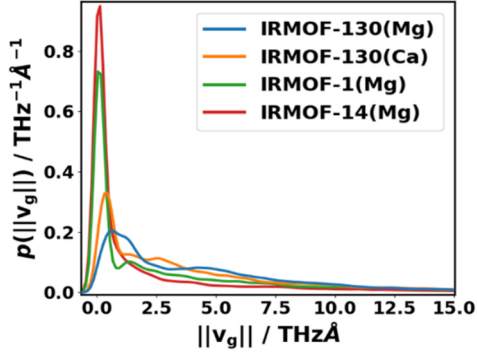


FIG. 12. Normalized density of group velocities for the studied systems.

F. Correlation between mode participation ratios and group velocities

In Sec. IV D, we have provided a rather qualitative discussion of the (partial) correlation between band dispersion and mode participation ratio (i.e., the localization of a vibration). In the following, this issue shall be addressed more quantitatively. Therefore, in Fig. 13 the correlations between the mode participation ratio and the group velocity of all phonons coinciding with the \mathbf{q} -grid specified in Sec. III C 2 are shown for the most “extreme” cases [IRMOF-130(Mg) and IRMOF-14(Mg)]. The data for the other two systems are contained in the Supplemental Material [21]. The frequency of each mode is included via a color code.

Fig. 13 highlights very clearly that there is no direct one-to-one correspondence between the localization of a vibration and the group velocity of the associated phonon. If such a direct correlation existed, all points would be grouped around a straight line through the origin. Rather the vast majority of the phonons have a group velocity below 20 THzÅ (consistent with Fig. 12) and participation ratios between 0.1 and 0.8.

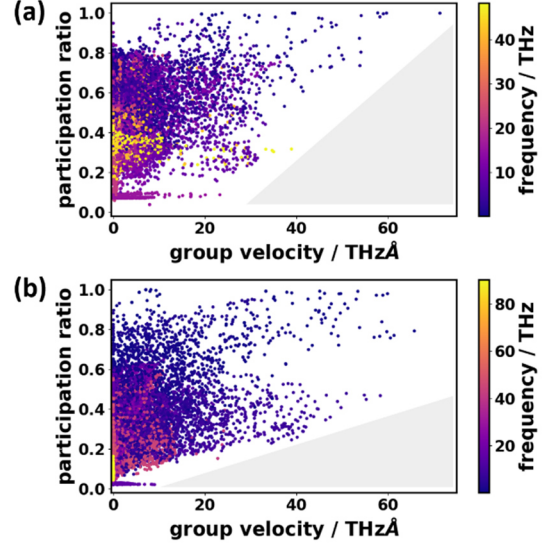


FIG. 13. Correlation between mode participation ratio and norm of the group velocity for all phonons considered in the determination of the densities of states. The frequency of each phonon is included via a color code. Panel (a) IRMOF-130(Mg) (calculated on a $12 \times 12 \times 12$ \mathbf{q} mesh) and (b) IRMOF-14(Mg) (calculated on a $10 \times 10 \times 10$ \mathbf{q} mesh). The grey triangles are a guide to the eye denoting a region with no modes.

Fig. 13, however, also shows that if the participation ratio is small, this limits the achievable group velocity (see grey-shaded triangles in Fig. 13). Notably, due to the longer linker in IRMOF-14(Mg) the size of the “forbidden region” is reduced, showing that in this very complex system also modes with relatively high group velocities but only moderate PRs exist.

V. SUMMARY AND CONCLUSION

We have analyzed the phonon properties of several prototypical isorecticular metal-organic frameworks. They turn out to be highly complex owing to the sheer number of phonon bands (138 bands even in the smallest considered system, IRMOF-130). Nevertheless, several general trends can be identified: the high-frequency region of the density of states is dominated by vibrations largely localized on the linker parts of the MOFs. Only for frequencies below ~ 20 THz, oscillations of the metal-oxide nodes start contributing significantly. As a consequence, the spectral weight of the density of states shifts to higher

frequencies for MOFs with more extended linkers. Notably for the latter systems (i.e., IRMOF-1 and IRMOF-14), the spectral region below ~ 3 THz is again dominated by vibrations involving primarily the linkers.

As far as the acoustic phonon bands are concerned, there are large differences in the band dispersions and group velocities between transverse and longitudinal modes, especially for propagation in the Γ -X direction (i.e., parallel to the linkers). This can be rationalized by the porous structure of the MOFs, which results in comparably weak restoring forces upon displacements perpendicular to the linker axes. Conversely, restoring forces for longitudinal acoustic displacements are sizable, as can be inferred from the rather large associated group velocities for long wavelengths. These, for the studied systems, range between 5000 ms^{-1} and 7700 ms^{-1} , comparable to and even exceeding many densely-packed solids. Notably, for the considered systems these group velocities for a given high-symmetry direction are largely independent of the chosen linker.

As far as the optical modes are concerned, even in the low-frequency region (up to ~ 3 THz) we observe a variety of different vibrations ranging from modes dominated by twisting motions of the nodes and torsional vibrations of the linkers, via linker bending modes of different order, to twisting modes of the carboxylic groups. Here we observe relations known from classical mechanics, like a proportionality of the frequencies of linker torsional motions to one over the square root of the torsional moment of inertia.

An observation relevant for all processes involving phonon transport in MOFs is that several of the optical phonons have sizable group velocities, although the highest group velocities are still observed for the longitudinal acoustic bands. With increasing linker complexity, one observes that the density of states with large group velocity diminishes,

and phonons with small group velocities become more abundant.

An interesting question for heterogeneous systems like MOFs is, whether there is a correlation between the (de)localization of a vibration (expressed via the mode participation ratio) and the group velocity of the associated phonon. Generally, we find that a one-to-one correspondence between these two quantities does not exist. Nevertheless, a sufficiently large mode participation ratio is a prerequisite for large group velocities. The opposite, namely that the group velocities for delocalized vibrations are always large is, however, not observed. On the one hand, this can be associated with standing-wave like displacements close to the Brillouin zone boundary. On the other hand, we find that for certain displacement patterns, the couplings between neighboring unit cells remain small, even if virtually all atoms of the MOF participate in the vibration.

These results highlight the rather complex correlation between MOF structure and phonon properties, but also show that promising properties, like high group velocities for acoustic, as well as optical phonons are well within reach in spite of the heterogeneous nature of the MOFs.

ACKNOWLEDGMENTS

Tomas Kamencek and Egbert Zojer acknowledge the Graz University of Technology for financial support through the Lead Project (LP-03) and the use of HPC resources provided by the ZID. The computational results have been in part achieved by using the Vienna Scientific Cluster (VSC3).

Natalia Bedoya gratefully acknowledges financial support under the COMET program within the K2 Center "Integrated Computational Material, Process and Product Engineering (IC-MPPE)" (Project No 859480). This program is supported by the Austrian Federal Ministries for Transport, Innovation and Technology (BMVIT) and for Digital and Economic Affairs (BMDW),

represented by the Austrian research funding association (FFG), and the federal states of Styria, Upper Austria and Tyrol.

-
- [1] J. Lee, O. K. Farha, J. Roberts, K. A. Scheidt, S. T. Nguyen, and J. T. Hupp, "Metal-organic framework materials as catalysts," *Chem. Soc. Rev.*, vol. 38, no. 5, pp. 1450–1459, 2009.
- [2] G. Ferey, "Hybrid porous solids: past, present, future.," *Chem. Soc. Rev.*, vol. 37, no. 1, pp. 191–214, Jan. 2008.
- [3] L. J. Murray, M. Dinca, and J. R. Long, "Hydrogen storage in metal-organic frameworks.," *Chem. Soc. Rev.*, vol. 38, no. 5, pp. 1294–1314, May 2009.
- [4] S. Keskin, T. M. van Heest, and D. S. Sholl, "Can metal-organic framework materials play a useful role in large-scale carbon dioxide separations?," *ChemSusChem*, vol. 3, no. 8, pp. 879–891, 2010.
- [5] T. A. Makal, J. R. Li, W. Lu, and H. C. Zhou, "Methane storage in advanced porous materials," *Chem. Soc. Rev.*, vol. 41, no. 23, pp. 7761–7779, 2012.
- [6] S. Kitagawa, R. Kitaura, and S. Noro, "Functional porous coordination polymers.," *Angew. Chem. Int. Ed. Engl.*, vol. 43, no. 18, pp. 2334–2375, Apr. 2004.
- [7] A. Ciupa and M. Ptak, "Polarized IR and Raman spectra of the novel metal-organic framework [CH₃CH₂NH₃][Cd(HCOO)₃]," *Vib. Spectrosc.*, vol. 86, pp. 67–74, 2016.
- [8] M. R. Ryder *et al.*, "Identifying the role of terahertz vibrations in metal-organic frameworks: From gate-opening phenomenon to shear-driven structural destabilization," *Phys. Rev. Lett.*, vol. 113, no. 21, pp. 1–6, 2014.
- [9] M. R. Ryder, B. Civalieri, G. Cinque, and J. C. Tan, "Discovering connections between terahertz vibrations and elasticity underpinning the collective dynamics of the HKUST-1 metal-organic framework," *CrystEngComm*, vol. 18, no. 23, pp. 4303–4312, 2016.
- [10] A. Krylov *et al.*, "Raman spectroscopy studies of the terahertz vibrational modes of a DUT-8 (Ni) metal-organic framework," *Phys. Chem. Chem. Phys.*, vol. 19, no. 47, pp. 32099–32104, 2017.
- [11] G. Kumari, K. Jayaramulu, T. K. Maji, and C. Narayana, "Temperature induced structural transformations and gas adsorption in the zeolitic imidazolate framework ZIF-8: A Raman study," *J. Phys. Chem. A*, vol. 117, no. 43, pp. 11006–11012, 2013.
- [12] L. H. N. Rimmer, M. T. Dove, A. L. Goodwin, and D. C. Palmer, "Acoustic phonons and negative thermal expansion in MOF-5," *Phys. Chem. Chem. Phys.*, vol. 16, no. 39, pp. 21144–21152, 2014.
- [13] X. Wang, R. Guo, D. Xu, J. Chung, M. Kaviani, and B. Huang, "Anisotropic Lattice Thermal Conductivity and Suppressed Acoustic Phonons in MOF-74 from First Principles," *J. Phys. Chem. C*, vol. 119, no. 46, pp. 26000–26008, 2015.
- [14] A. Kuc, A. Enyashin, and G. Seifert, "Metal-organic frameworks: Structural, energetic, electronic, and mechanical properties," *J. Phys. Chem. B*, vol. 111, no. 28, pp. 8179–8186, 2007.
- [15] H. Li, M. Eddaoudi, M. O’Keeffe, and O. M. Yaghi, "Design and synthesis of an exceptionally stable and highly porous metal-organic framework," *Nature*, vol. 402, p. 276, Nov. 1999.
- [16] D. F. Bahr *et al.*, "Mechanical properties of cubic zinc carboxylate IRMOF-1 metal-organic framework crystals," *Phys. Rev. B - Condens. Matter Mater. Phys.*, vol. 76, no. 18, pp. 1–7, 2007.
- [17] L. M. Yang, P. Ravindran, P. Vajeeston, and M. Tilset, "Properties of IRMOF-14 and its analogues M-IRMOF-14 (M = Cd, alkaline earth metals): Electronic structure, structural stability, chemical bonding, and optical properties," *Phys. Chem. Chem. Phys.*, vol. 14, no. 14, pp. 4713–4723, 2012.
- [18] L. M. Yang, P. Vajeeston, P. Ravindran, H. Fjellvåg, and M. Tilset, "Revisiting isorecticular MOFs of alkaline earth metals: A comprehensive study on phase stability, electronic structure, chemical bonding, and optical properties of A-IRMOF-1 (A = Be, Mg, Ca, Sr, Ba)," *Phys. Chem. Chem. Phys.*, vol. 13, no. 21, pp. 10191–10203, 2011.
- [19] L.-M. Yang, P. Ravindran, P. Vajeeston, and M. Tilset, "Ab initio investigations on the crystal structure, formation enthalpy, electronic structure, chemical bonding, and optical properties of experimentally synthesized isorecticular metal-organic framework-10 and its analogues: M-

- IRMOF-10 (M = Zn, Cd, Be, Mg, ,” *RSC Adv.*, vol. 2, no. 4, pp. 1618–1631, 2012.
- [20] C. Somboon, Y. C. Zhou Kui, L. Zhixiong, and V. Francis, “Alkali-Metal Tuning of Adsorption Sites in Metal Organic Frameworks MOF-5 for Carbon Dioxide/Methane Separation at Ambient Conditions,” *Chinese J. Appl. Chem.*, vol. 32, no. 5, pp. 552–556, 2015.
- [21] See Supplemental Material for a detailed descriptions of the technical problems with IRMOF-1(Zn), the simulation parameters in VASP and DFTB+, the geometry optimization procedure, effect of vdW or DFTB3 correction, supercell convergence behavior, further DFTB benchmarks, dependence of the PES with respect to the torsional mode of carboxylic oxygen, sound velocity data, 1-d group velocity density, correlation between group velocity and mode localisation for the remaining systems
- [22] P. Hohenberg and W. Kohn, “Inhomogeneous Electron Gas,” *Phys. Rev.*, vol. 136, no. 3B, pp. B864–B871, Nov. 1964.
- [23] W. Kohn and L. J. Sham, “Self-Consistent Equations Including Exchange and Correlation Effects,” *Phys. Rev.*, vol. 140, no. 4A, pp. A1133–A1138, Nov. 1965.
- [24] G. Kresse and J. Hafner, “Ab initio molecular dynamics for liquid metals,” *Phys. Rev. B*, vol. 47, no. 1, pp. 558–561, Jan. 1993.
- [25] G. Kresse and J. Hafner, “Ab initio molecular-dynamics simulation of the liquid-metal–amorphous-semiconductor transition in germanium,” *Phys. Rev. B*, vol. 49, no. 20, pp. 14251–14269, May 1994.
- [26] G. Kresse and J. Furthmüller, “Efficiency of ab-initio total energy calculations for metals and semiconductors using a plane-wave basis set,” *Comput. Mater. Sci.*, vol. 6, no. 1, pp. 15–50, 1996.
- [27] G. Kresse and J. Furthmüller, “Efficient iterative schemes for ab initio total-energy calculations using a plane-wave basis set,” *Phys. Rev. B*, vol. 54, no. 16, pp. 11169–11186, Oct. 1996.
- [28] J. P. Perdew, K. Burke, and M. Ernzerhof, “Generalized Gradient Approximation Made Simple,” *Phys. Rev. Lett.*, vol. 77, no. 18, pp. 3865–3868, Oct. 1996.
- [29] P. E. Blöchl, “Projector augmented-wave method,” *Phys. Rev. B*, vol. 50, no. 24, pp. 17953–17979, Dec. 1994.
- [30] G. Kresse and D. Joubert, “From ultrasoft pseudopotentials to the projector augmented-wave method,” *Phys. Rev. B*, vol. 59, no. 3, pp. 1758–1775, Jan. 1999.
- [31] G. Seifert, D. Porezag, and T. Frauenheim, “Calculations of molecules, clusters, and solids with a simplified LCAO-DFT-LDA scheme,” *Int. J. Quantum Chem.*, vol. 58, no. 2, pp. 185–192, 1996.
- [32] A. F. Oliveira, G. Seifert, T. Heine, and H. A. Duarte, “Density-functional based tight-binding: an approximate DFT method ,” *Journal of the Brazilian Chemical Society* , vol. 20. scielo , pp. 1193–1205, 2009.
- [33] D. Porezag, T. Frauenheim, T. Köhler, G. Seifert, and R. Kaschner, “Construction of tight-binding-like potentials on the basis of density-functional theory: Application to carbon,” *Phys. Rev. B*, vol. 51, no. 19, pp. 12947–12957, May 1995.
- [34] T. Frauenheim *et al.*, “A Self-Consistent Charge Density-Functional Based Tight-Binding Method for Predictive Materials Simulations in Physics, Chemistry and Biology,” *Phys. status solidi*, vol. 217, no. 1, pp. 41–62, Jan. 2000.
- [35] B. Lukose *et al.*, “Structural properties of metal-organic frameworks within the density-functional based tight-binding method,” *Phys. Status Solidi Basic Res.*, vol. 249, no. 2, pp. 335–342, 2012.
- [36] B. Aradi, B. Hourahine, and T. Frauenheim, “DFTB+, a Sparse Matrix-Based Implementation of the DFTB Method,” *J. Phys. Chem. A*, vol. 111, no. 26, pp. 5678–5684, Jul. 2007.
- [37] M. Gaus, A. Goez, and M. Elstner, “Parametrization and Benchmark of DFTB3 for Organic Molecules,” *J. Chem. Theory Comput.*, vol. 9, no. 1, pp. 338–354, Jan. 2013.
- [38] M. Kubillus, T. Kubař, M. Gaus, J. Řezáč, and M. Elstner, “Parameterization of the DFTB3 Method for Br, Ca, Cl, F, I, K, and Na in Organic and Biological Systems,” *J. Chem. Theory Comput.*, vol. 11, no. 1, pp. 332–342, Jan. 2015.
- [39] X. Lu, M. Gaus, M. Elstner, and Q. Cui, “Parametrization of DFTB3/3OB for Magnesium and Zinc for Chemical and Biological Applications,” *J. Phys. Chem. B*, vol. 119, no. 3, pp. 1062–1082, Jan. 2015.
- [40] M. Gaus, Q. Cui, and M. Elstner, “DFTB3: Extension of the Self-Consistent-Charge Density-Functional Tight-Binding Method (SCC-DFTB),” *J. Chem. Theory Comput.*, vol. 7, no. 4, pp. 931–948, Apr. 2011.
- [41] A. Togo and I. Tanaka, “First principles phonon calculations in materials science,” *Scr. Mater.*, vol. 108, pp. 1–5, 2015.

- [42] K. Momma and F. Izumi, "VESTA 3 for three-dimensional visualization of crystal, volumetric and morphology data," *J. Appl. Crystallogr.*, vol. 44, no. 6, pp. 1272–1276, 2011.
- [43] R. J. Bell, P. Dean, and D. C. Hibbins-Butler, "Localization of normal modes in vitreous silica, germania and beryllium fluoride," *J. Phys. C Solid State Phys.*, vol. 3, no. 10, pp. 2111–2118, 1970.
- [44] J. T. Edwards and D. J. Thouless, "Numerical studies of localization in disordered systems," *J. Phys. C Solid State Phys.*, vol. 5, no. 8, pp. 807–820, 1972.
- [45] J. Canisius and J. L. van Hemmen, "Localisation of phonons," *J. Phys. C Solid State Phys.*, vol. 18, no. 25, pp. 4873–4884, 1985.
- [46] G. D. Barrera, J. A. O. Bruno, T. H. K. Barron, and N. L. Allan, "Negative thermal expansion," *J. Phys. Condens. Matter*, vol. 17, no. 4, 2005.
- [47] W. Zhou, H. Wu, T. Yildirim, J. R. Simpson, and A. R. H. Walker, "Origin of the exceptional negative thermal expansion in metal-organic framework-5 $Zn_4O(1,4\text{-benzenedicarboxylate})_3$," *Phys. Rev. B - Condens. Matter Mater. Phys.*, vol. 78, no. 5, pp. 1–5, 2008.
- [48] D. Dubbeldam, K. S. Walton, D. E. Ellis, and R. Q. Snurr, "Exceptional negative thermal expansion in isorecticular metal-organic frameworks," *Angew. Chemie - Int. Ed.*, 2007.
- [49] N. Lock *et al.*, "Elucidating negative thermal expansion in MOF-5," *J. Phys. Chem. C*, vol. 114, no. 39, pp. 16181–16186, 2010.
- [50] L. Wang, C. Wang, Y. Sun, K. Shi, S. Deng, and H. Lu, "Large negative thermal expansion provided by metal-organic framework MOF-5: A first-principles study," *Mater. Chem. Phys.*, vol. 175, pp. 138–145, 2016.
- [51] N. Lock *et al.*, "Scrutinizing negative thermal expansion in MOF-5 by scattering techniques and ab initio calculations," *J. Chem. Soc. Dalton Trans.*, vol. 42, no. 2, pp. 1996–2007, 2013.
- [52] C. Kittel, *Introduction to Solid State Physics*. Wiley, 2004.